2025 International Conference on Manipulation, Automation and Robotics at Small Scales (MARSS) | 979-8-3315-9687-3/25/$31.00 ©2025 IEEE | DOI: 10.1109/MARSS65887.2025.11072509

Electromagnetic Objective Lens Scanner: Design, Modeling and Characterization*

Yuen K. Yong, Ben S. Routley, Andrew J. Fleming

***Abstract*— This article describes an electromagnetic objective lens positioner for applications that require millimeter scale vertical travel and wide bandwidth, such as Michelson interferometry, laser micromachining, and confocal microscopy. The proposed device is a cylindrical Lorentz actuator with a stationary permanent magnet and moving coil. The motion of the objective is guided by two planar flexures that determine the travel range, stiffness and resonance frequency. The travel range can be easily varied, e.g. from 100 μm to 1 mm, by altering the flexure dimensions. Analytical solutions for the stiffness, travel range and resonance frequency are derived and validated by finite-element analysis and experimental results. Compared to existing piezoelectric objective scanners, the proposed electromagnetic scanner exhibits higher linearity in open-loop, lower temperature dependence, can operate in humid environments, and has a reconfigurable travel range. The disadvantages compared to a piezoelectric scanner include heat dissipation for static displacement, the possibility of stray magnetic fields, lower lateral stiffness, and larger physical size. However, although the volume is larger than an equivalent piezoelectric scanner, the cylindrical shape is suited to many microscope turrets.**

Fig. 1. Assembled and exploded views of the objective scanner.

I. Introduction

Objective scanners with millimeter scale travel range and high precision are required in numerous microscopy and industrial applications. In scanning interferometry [1]–[3], laser material processing [4], [5], confocal microscopy and two-photon microscopy [6], [7], objective scanners are used to move an objective lens along its optical axis to change the focal length.

This article describes a high-speed objective scanner driven by a voice coil actuator (VCA). The VCA-driven scanner uses a radially poled magnet and a tubular coil of wire to minimize flux leakage and maximize linearity over the travel range [8], [9].

Many commercial objective scanners are driven by piezoelectric actuators, including the P-725 and P-726 from Physik Instrumente [10], PFM450E from Thorlabs [11], Nano Scan OP400 from Prior Scientific [12], and the P70 and XD7 series from CoreMorrow [13]. Piezoelectric stack actuators are compact and capable of providing high force and high bandwidth to drive a positioner [14]–[19]. In high-speed systems, flexures with high stiffness along the actuation axis are required to preload the piezoelectric stack actuators [20], [21]. These flexures are also used to increase the first resonance frequency of the system, and to achieve a large control bandwidth [22]. However, a disadvantage of stiff flexures is a strict trade-off between range and bandwidth [19], [22]. Lorentz or voice coil actuators (VCAs) have been used for precision positioning to achieve a relatively large travel range, from hundreds of microns to a few milimeters [9], [23]–[26]. Unlike piezoelectric actuators with hysteresis, VCAs have a linear relationship between input current and output force, which is ideal for generating linear motion. Increasing the first resonance frequency of VCA-driven positioners is relatively simple compared to piezoelectric-driven systems, due to the high stiffness and small maximum strain (0.1%) of piezoelectric actuators [22]. The first and second resonance modes of piezoelectric stack actuators are typically bending modes that arise from their slender structurs [27]. To avoid these modes, flexures with high stiffness along the uncontrollable axes are required to restrict motion and increase the resonance frquency above the resonance frequency of the actuation axis [22], [27]–[29]. For VCA-driven positioners, the stiffness of the structure is only a function of the flexures, which simplifes the design procedure significantly. The first resonance frequency along the actuation axis can be increased by simply increasing the flexure stiffness, e.g. by increasing the thickness.

Section II describes the design and construction of the objective scanner. The stiffness, resonance frequency, and electromagnectic sensitivity are then derived analytically in Section III. Section IV presents finite-element analysis in the mechanical and electromagnetic domains. Experimental

*This work was supported by the Australian Research Council Discovery Grant DP170101813. The authors are with the School of Engineering, University of Newcastle, Callaghan, NSW 2308, Australia. yuenkuan.yong@newcastle.edu.au

979-8-3503-7680-7 ©2024 IEEE

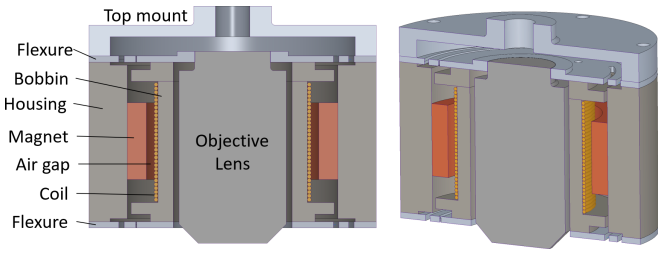

Fig. 2. Sectional view of the objective scanner.

results are presented in Section V, followed by an example interferometer application in Section VI. Section VII concludes the work.

II. System Description

As shown in Figure 1, the proposed objective scanner is constructed from two aluminium plate flexures (top and bottom), a cylindrical permanent magnet, a steel bobbin, a steel cylindrical housing, a stainless steel top mount and an objective lens. The permanent magnet is embedded on the inside diameter of the cylindrical housing, and the tubular coil of wire is wrapped around the bobbin and situated within a radially oriented magnetic field, as depicted in Figure 2. An air gap is formed between the magnet and coil. The objective lens is situated in the center of the hollow structure and mounted to the top flexure which has a Royal Microscopy Society (RMS) thread, as shown in Figure 3. The bobbin is mounted to the plate flexures via five inner mounting holes. The flexures are then secured to the cylindrical housing via five outer mounting holes. When current is applied to the coil, the induced magnetic force deforms the plate flexures to generate axial motion.

III. Modeling

Each plate flexure consists of five identical curved beams as shown in Figure 3. The flexures are made of aluminium alloy (Al7072) with a thickness t of 1.6 mm. Each curved beam has a width h of 2.8 mm, a radius of curvature R of 29.5 mm, and a curve angle ϕ_o of 55.5°. Dimensions and material properties are summarized in Tables I and II.

TABLE I
Dimensions and component mass of the scanner.

Dimensions

Description	Parameter	Value
Beam thickness [mm]	t	1.6
Beam width [mm]	h	2.8
Radius of curvature [mm]	R	29.5
Curve angle (span) [°]	ϕ_o	55.5

Mass

Description	Parameter	Value [kg]
Bobbin	m_c	0.186
Magnet	m_m	0.15
Objective lens	m_l	0.22
Central platform of flexure	m_p	0.02

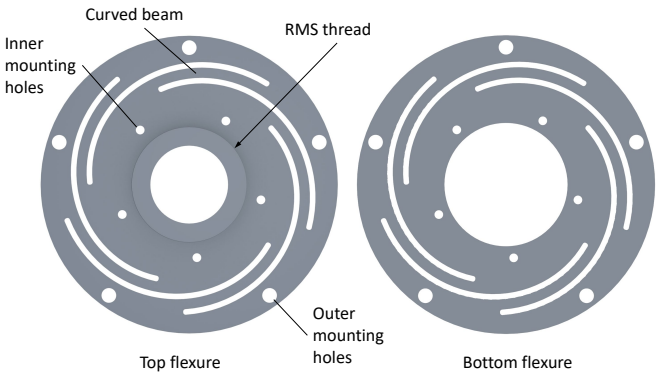

Fig. 3. Top and bottom plate flexures.

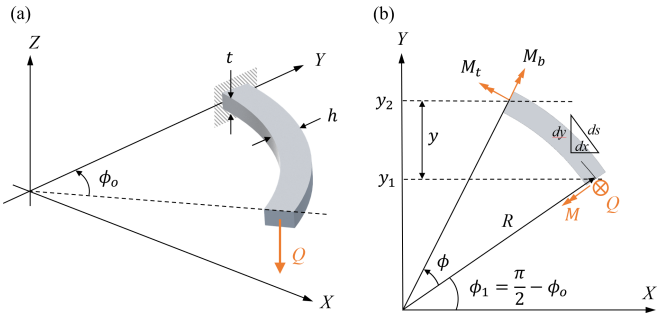

Fig. 4. (a) Curved-beam model with parametric dimensions, loads and boundary conditions. (b) The cross-sectional bending and torsional moments, and the beam element.

A. Effective Stiffness

To model the effective stiffness of the scanner with curved beams, the elastic strain energy and Castigliano's second theorem are used [20], [30]–[32]. As depicted in Figure 4, the equilibrium of moment along the x and y directions are [28], [32],

$$\begin{aligned} &M_b\cos(\phi+\phi_1)-M_t\sin(\phi+\phi_1)-M\cos(\phi_1)+Qy=0\\ &M_b\sin(\phi+\phi_1)+M_t\cos(\phi+\phi_1)-M\sin(\phi_1)+Q(x_o-x)\\ &=0, \end{aligned} \tag{1}$$

where $y = R\sin(\phi+\phi_1) - R\sin(\phi_1)$, $x = R\cos(\phi+\phi_1)$, and $x_o = R\cos(\phi_1)$. Q is the shear force on the curved beam. Solving (1) for M_b and M_t gives,

$$\begin{aligned} M_b &= M\cos\phi - QR\sin\phi\\ M_t &= QR - M\sin\phi - QR\cos\phi. \end{aligned} \tag{2}$$

The elastic strain energy stored in each beam is,

$$U = \frac{1}{2EI}\int^L M_b^2 ds + \frac{1}{2GJ}\int^L M_t^2 ds, \tag{3}$$

where E is Young's modulus, I is second moment of inertia, G is shear modulus, J is polar moment of inertia, and L is the length of the beam. The integration is performed with respect to the length of a beam element ds. Because of the guided boundary condition of the beam, the slope of the

TABLE II

MATERIAL PROPERTIES OF EACH COMPONENT IN THE SCANNER.

Component	Material	Young Modulus E, [GPa]	Shear Modulus G, [GPa]	Poisson's ratio	Density ρ, [kg/m^3]	Relative Permeability	Others
Top mount	Stainless steel	200	77	0.3	7850	1	
Plate flexure	Al7072	72	27	0.33	2770	1	
Bobbin	Steel	193	74	0.31	7750	B-H curve	
Outer housing	Steel	193	74	0.31	7750	B-H curve	
Coil	Copper	120	41	0.38	8300	1	169 turns, 3 layers
Magnet	NdFe35	147	–	–	7400	B-H curve	Coercivity = 890 kA/m

beam Θ is zero where the shear force Q is acting. Using Castigliano's theorem, and exploiting $\Theta = 0$ results in,

$$\Theta = \frac{\partial U}{\partial M} = 0 \quad = \quad \frac{1}{2EI}\int^{L} 2M_b \frac{\partial M_b}{\partial M} ds + \frac{1}{2GJ}\int^{L} 2M_t \frac{\partial M_t}{\partial M} ds. \tag{4}$$

Substituting (2), $\partial M_b/\partial M$, $\partial M_t/\partial M$, and $ds = Rd\phi$ into (4), and performing integration from $\frac{\pi}{2} - \phi_o$ to $\frac{\pi}{2}$ (the span of the curved beam) gives,

$$\frac{Q\,R^2 \sin(\phi_o)^2 - 2\,Q\,R^2\,\sin(\phi_o) + 2\,M\left(\frac{\phi_o}{2} + \frac{\sin(2\,\phi_o)}{4}\right)R}{2\,G\,J} - \frac{Q\,R^2 \sin(\phi_o)^2 - 2\,M\,R\left(\frac{\phi_o}{2} - \frac{\sin(2\,\phi_o)}{4}\right)}{2\,E\,I} = 0 \tag{5}$$

Simplifying the above equation and solving for M,

$$M = \frac{2QR\sin\phi_o(2EI - EI\sin\phi_o + GJ\sin\phi_o)}{EI\sin(2\phi_o) - GJ\sin(2\phi_o) + 2EI\phi_o + 2GJ\phi_o}. \tag{6}$$

Knowing M, the deflection δ of the beam can be determined. Using Castigliano's theorem results in,

$$\delta = \frac{\partial U}{\partial Q} \quad = \quad \frac{1}{2EI}\int^{L} 2M_b \frac{\partial M_b}{\partial Q} ds + \frac{1}{2GJ}\int^{L} 2M_t \frac{\partial M_t}{\partial Q} ds. \tag{7}$$

Similarly, entering M_b, $\partial M_b/\partial Q$, M_t, $\partial M_t/\partial Q$, and $ds = Rd\phi$ into (7), and performing integration from $\frac{\pi}{2} - \phi_o$ to $\frac{\pi}{2}$ gives,

$$\delta = \frac{1}{GJ}\left[2QR^3(\cos\phi_o - 1) - MR^2\sin\phi_o + \frac{MR^2\sin^2\phi_o}{2} + QR^3\left(\frac{\phi_o}{2} - \frac{\cos\phi_o\sin\phi_o}{2}\right) + QR^3\phi_o\right] + \frac{1}{EI}\left[QR^3\left(\frac{\phi_o}{2} + \frac{\sin(2\phi_o)}{4}\right) - \frac{MR^2\sin^2\phi_o}{2}\right]. \tag{8}$$

With the dimensions and material properties given in Tables I and II, and by substituting (6) into (8), the deflection of the fixed-guided curved beam is $\delta = 40.54Q$. The predicted stiffness is $k_b = Q/\delta = 0.0216$ N/μm. Since each plate flexure consists of five curved beams arranged in parallel, two plate flexures provide a total stiffness of $k_T = 10k_b = 0.2$ N/μm.

B. Resonance Frequency

To estimate the resonance frequency of the objective scanner, the effective mass of the flexures is first calculated using the Rayleigh's principle [31], [33],

$$m_{eff} \quad = \quad \rho A\int^{L}\left[\frac{\delta}{\delta_{max}}\right]^2 dx = \rho A\int_{\frac{\pi}{2}-\phi_o}^{\frac{\pi}{2}}\left[\frac{\delta}{\delta_{max}}\right]^2 Rd\phi \tag{9}$$

where $A = ht$ is the cross-sectional area of the beam, and ρ is the density. By performing numerical integration to (9), the effective mass for each curved beam is $m_{eff} = 0.0052$ kg. The total effective mass M_e is the sum of $10\,m_{eff}$, the mass of bobbin m_c, magnet m_m, objective lens m_l and the middle platform of the plate flexures m_p, as tabulated in Table I. The estimated effective mass is $M_e = 0.58$ kg. The resonance frequency of the objective scanner is,

$$f_{res} = \frac{1}{2\pi}\sqrt{\frac{k_T}{M_e}}. \tag{10}$$

The calculated first resonance frequency of the scanner is $f_{res} = 93.6$ Hz.

C. Electromagnetic Actuation

The electromagnetic actuator is illustrated in Figures 1 and 2, where a stationary radially polarized magnet creates a uniform magnetic flux through a portion of a moving coil. When a current is passed through the coil, a Lorentz force acts in the vertical direction which displaces the objective and guiding flexural springs.

Dimensions of the magnetic components are described in Figure 5(a). To minimize non-linearity due to fringing fields, the coil length is chosen to be significantly longer than the magnet so that almost all of the magnetic flux passes through the coil, regardless of deflection. The air-gaps above the coil, and at either end of the bobbin are minimized to 1 mm, which is constrained by fabrication and assembly tolerances.

The coil was designed to utilize the available volume and provide a convenient resistance for a +/-10 V linear amplifier. 169 turns of 0.55 mm insulated copper wire were wound in three layers on the bobbin, which is 39 mm diameter and 31.6 mm long. This required approximately 21 m of wire, and resulted in a 2.4 Ohm resistance, which is well suited to the output voltage and current range of the linear amplifier (+/-10 V and +/-5 Amps).

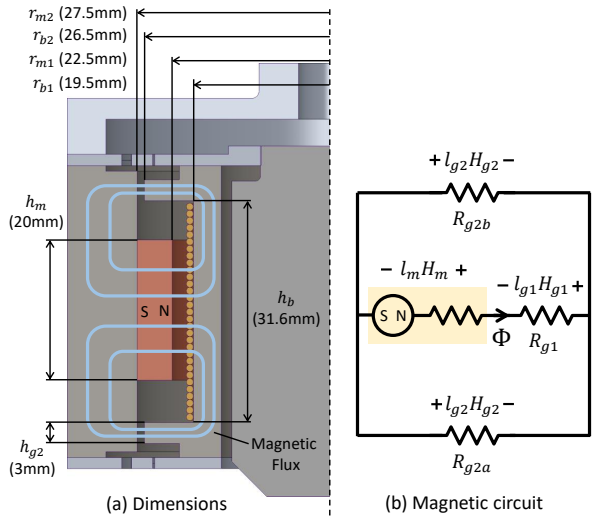

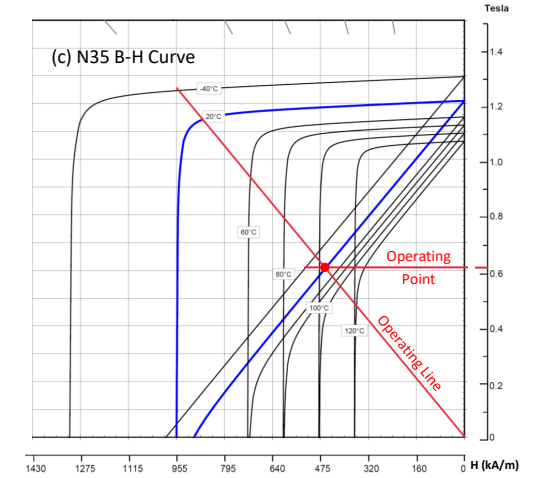

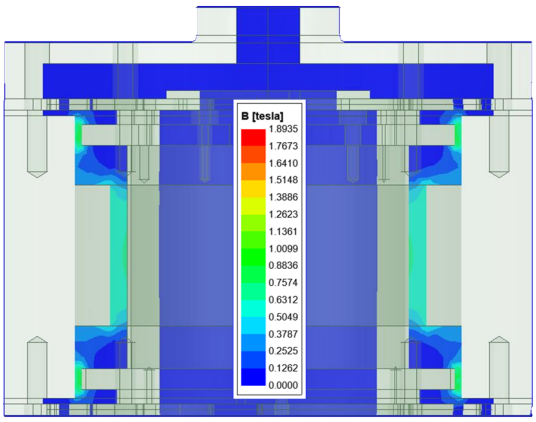

(d) FEA Simulation of flux density (plotted in air gaps)

Fig. 5. Electromagnetic dimensions (a), model (b), magnetic material properties (c), and FEA simulation results (d).

To determine the relationship between the applied current and developed force, the magnetic flux in the portion of the exposed coil must be determined. The equivalent magnetic circuit is shown in Figure 5(b) where the magnet is represented by the shaded MMF source and reluctance, and the air-gaps are represented by R_{g1}, R_{g2a}, and R_{g2b}. The reluctance of steel components are assumed to be negligible compared to the the air-gaps.

The reluctance between the magnet North pole and the bobbin R_{g1} is

$$R_{g1} = \frac{l_{g1}}{\mu_0 A_{g1}} = 904.65 \times 10^3 \text{ H}^{-1}, \tag{11}$$

where the gap length is $l_{g1} = r_{m1} - r_{b1}$, and the area is $A_{g1} = h_m 2\pi \frac{r_{m1}+r_{b1}}{2}$. The reluctances R_{g2a} and R_{g2b} of the flux return air-gaps appear in parallel and can be modeled as a single reluctance R_{g2}, i.e.

$$R_{g2} = \frac{l_{g2}}{\mu_0 A_{g2}} = 301.55 \times 10^3 \text{ H}^{-1}, \tag{12}$$

where $l_{g2} = r_{m2} - r_{b2}$, and $A_{g2} = 2h_{g2}2\pi \frac{r_{m2}+r_{b2}}{2}$.

By applying Ampere's law [34], the MMF drop around the magnetic loop is equal to zero, and can be written either in terms of the MMF, or the magnetic flux Φ and reluctance R since MMF $= \Phi R$, i.e.

$$l_mH_m = -\left(l_{g1}H_{g1} + l_{g2}H_{g2}\right), \tag{13}$$

$$l_mH_m = -\Phi(R_{g1} + R_{g2}). \tag{14}$$

where l_m, l_{g1}, and l_{g2} are the magnetic paths lengths, and H_m, H_{g1}, and H_{g2} are the magnetic field strengths in the magnet and air gaps.

An identical flux Φ flows through the magnet and air gaps R_{g1} and R_{g2}, i.e.

$$\Phi = B_mA_m = B_{g1}A_{g1} = B_{g2}A_{g2}, \tag{15}$$

where B_m, B_{g1}, and B_{g2} are the flux densities in the magnet and air gaps. By substituting $\Phi = B_mA_m$ into Equation 14, and rearranging, the relationship between flux density and magnetic field can be determined, i.e.

$$H_m = \frac{-A_m(R_{g1} + R_{g2})}{l_m} B_m = -758880\ B_m. \tag{16}$$

This equation describes the operating line of the magnetic circuit and can be solved simultaneously with an expression for the magnet B_m and H_m. In practice, this can be performed graphically using the B-H curve for NdFeB-N35 [35], which is plotted in Figure 5(c), where the operating line intersects the room temperature curve for the magnet at $B_m^* = 0.625$ T. Assuming a uniform flux density, the flux density in the area of the coil covered by the magnet is also $B_{g1} = 0.625$ T.

Since the magnetic field is perpendicular to the wire, the Lorentz force acting on the coil is [34],

$$F_Z = l_wB_{g1}I_w = \frac{Nh_m}{h_b} 2\pi(r_{b1} + 1.5D_w)B_{g1}I_w, \tag{17}$$

where l_w is the wire length exposed to the field, Nh_m/h_b is the number of turns exposed to the field (107), $2\pi(r_{b1} + 1.5D_w)$ is the average length of wire in one turn of a three layer coil, D_w is the wire diameter, and I_w is the applied current. Evaluating this expression results in

$$\frac{F_Z}{I_w} = 8.54 \text{ Newtons per Amp} \tag{18}$$

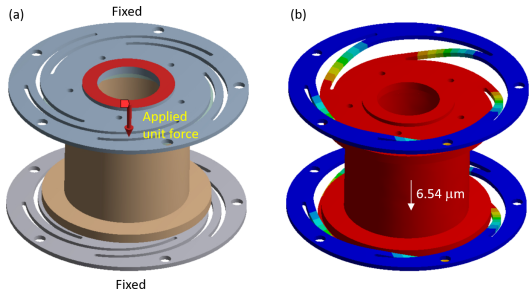

Fig. 6. Boundary conditions for the finite-element model. (a) The cylindrical housing and top mount (not shown) are fixed. A unit force was applied to the middle of top plate flexure. (b) Simulated deformation of the scanner.

Based on the flexural stiffness measured in Section V ($k = 0.155$ N/μm), the expected displacement per Amp is

$$\frac{d_Z}{I_w} = \frac{F_Z}{I_w}\frac{1}{k} = 55.09\ \mu\text{m/A}. \tag{19}$$

In Section V, the experimental sensitivity was measured to be 52.3 μm/A, which is 5.05% below the predicted value. The discrepancy is attributed to tolerance of the magnetic depolarization curve reported in the datasheet.

IV. Finite-element Modeling

ANSYS Workbench is used to construct a finite-element model of the objective scanner to simulate its stiffness and resonance frequency. Maxwell 3D within the ANSYS Workbench is used to simulate the magnetic flux density and the generated force. Material properties of the model are listed in Table II. Boundary conditions are shown in Figure 6(a).

A. Stiffness and resonance frequencies

To simulated the stiffness, a unit force is applied to the top plate flexure shown in Figure 6(b). The simulated deformation of the scanner is 6.54 μm, which equates to stiffness of 0.153 N/μm.

Resonance frequencies of the scanner are simulated using the same boundary conditions without the unit force applied. The objective lens is modeled as a metal object with a mass of 220 g. The first simulated resonance frequency is the vertical mode at 95 Hz, which is in close agreement to the analytical value of 93.6 Hz. Figure 7 shows the first six resonant modes of the objective scanner.

B. Magnetic Flux Density and Displacement

The flux density is simulated using Maxwell 3D within ANSYS Workbench. Magnetic material properties are listed in Table II. The flux density in the air gaps are plotted in Figure 5(d). The resulting flux density in the middle of the coil is 0.66 T, which is 5.6% greater than the value predicted in Section III-C.

The simulated force distribution on the coil in Maxwell 3D is transferred as load into ANSYS Mechanical to enable coupling between the two domains. The displacement of the objective scanner is solved in ANSYS Mechanical.

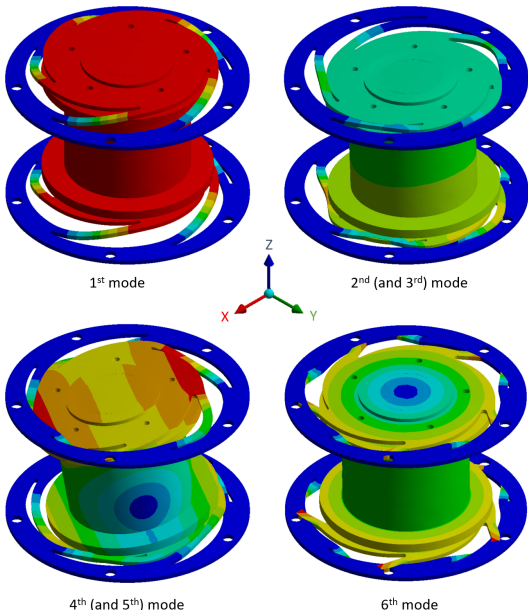

Fig. 7. Simulated resonance frequencies of the objective scanner. The first resonance mode is the vertical mode at 95 Hz. The second and third modes are the lateral modes along the x- and y-axis respectively at 695 Hz. The fourth and fifth modes rotate about the x and y axes respectively at 915.4 Hz. The sixth mode is a twisting mode that rotates about the z-axis at 1845.6 Hz. Note that the third and fifth modes are not shown as these modes are similar to the second and fourth modes, respectively.

TABLE III
Comparison of Analytical, FE and Experimental Results.

Description	Analytical	FE	Exp
Stiffness [N/μm]	0.2	0.153	0.155
First res. freq. [Hz]	93.6	95	106.9
Disp. gain [μm/A]	42.7	42	52.3

For an applied current of 6 A, the obtained displacement is 252.1 μm, which amounts to a displacement gain of 42 μm/A.

V. Experimental Results

The frequency response, travel range and cross-coupling of the objective scanner was characterized using the experimental setup depicted in Figure 8. The scanner was mounted on a vibration isolation table with the lens facing upwards. A Polytec PSV-300 laser scanning vibrometer was used to measure the x-, y- and z-axis frequency responses and displacements of the objective lens. A pseudorandom signal of 100 mVpk and 2 kHz bandwidth was applied to a current amplifier with a gain of 2 A/V. The measured frequency responses from the z input (in Amps) to the output displacements (in μm) along the x-, y- and z-axis are plotted in Figure 9. The first mechanical resonance mode is the expected vertical mode along the z-axis at 106.9 Hz.

The travel range and cross-coupling motions are measured by applying a 10 Hz, 6 A peak-to-peak sinusoidal current to the scanner. The measured x, y and z displacements are plotted in Figure 10. The z-axis travel range is 314 μm, which is 52.3 μm/A. The cross-coupling is 10.4 μm (3.3%) in

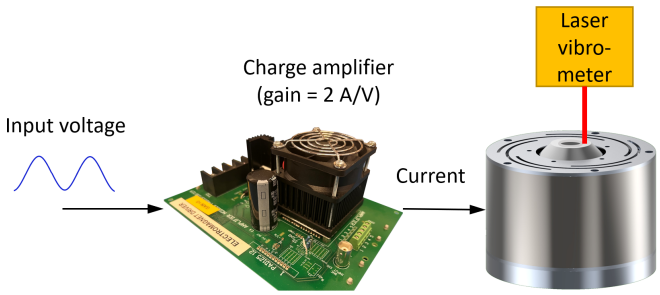

Fig. 8. Experimental setup for measuring frequency responses and travel range.

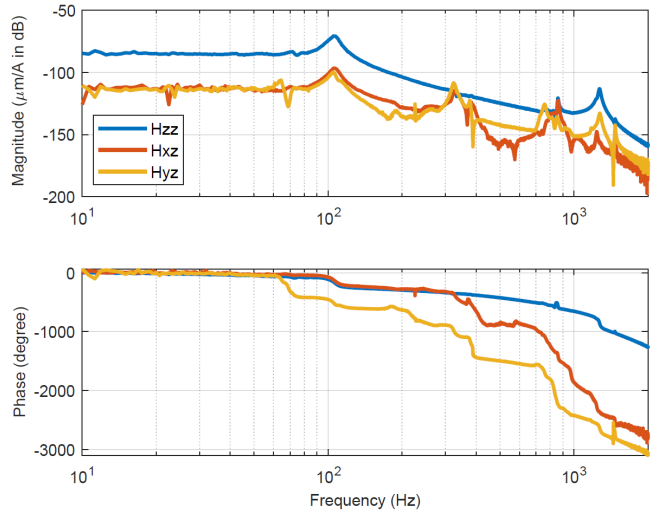

Fig. 9. Frequency responses of the objective scanner. H_{xz}, H_{yz} and H_{zz} are the frequency responses from input z to output x, y, and z, respectively.

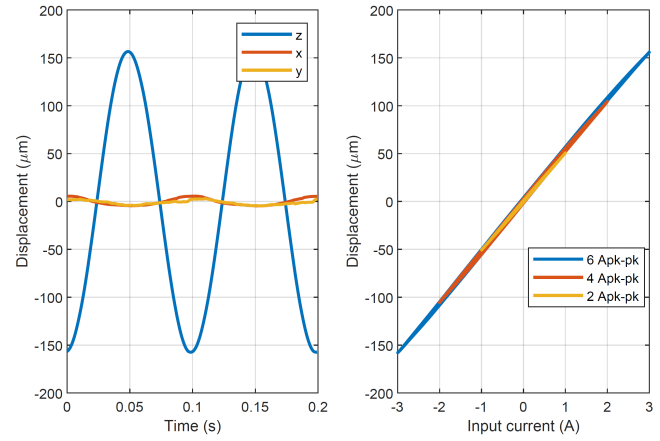

Fig. 10. (Left) Travel range in the z-axis and cross-coupling motions in the x- and y-axis. (Right) Hysteresis plots with a 2-A peak-to-peak, 4-A peak-to-peak and 6-A peak-to-peak sinusoidal input.

the x-axis and 7.6 μm (2.4%) in the y-axis. Hysteresis plots of the scanner with a 2-A peak-to-peak, 4-A peak-to-peak and 6-A peak-to-peak sinusoidal input are also presented in Figure 10. The hysteresis loop is approximately 2% of the maximum displacement in all three cases. The analyical, finite-element, and experimental results are compared in Table III, which shows acceptable agreement.

VI. Interferometer-based Atomic Force Microscopy

To demonstrate the functionality of the proposed objective scanner, a phase-locked Michelson micro interferometer was constructed using a Nikio 10X Mirau objective [36], as shown in Figure 11. The interferometer was used to measure the frequency response and thermal noise of an atomic force microscope microcantilever probe, which also creates an interferometer-based atomic force microscope deflection sensor.

Figure 11 shows an overview of the experimental setup. A fibre-coupled 635-nm distributed feedback laser is collimated, then directed through a 50:50 beam splitter. Half of the split beam is dumped, and the remaining portion is focused through a Mirau objective lens onto an AFM probe, forming a Michelson interferometer. The light returned from the objective lens is passed through the beam splitter. Half of the returned beam is dumped into the collimator, and the power in the remaining portion is measured by a Thorlab's PDA36A-EC photodiode. An SRS SIM960 analogue PID controller drives the objective scanner until the phase of the interferogram is $3\pi/2$, i.e. the zero-crossing point where small deviations in path length are proportional to the measured intensity [36]. forming the feedback loop to lock the interferometer's phase.

Using the interferometer in Figure 11, the frequency response and thermal noise of the microcantilever were measured using the signal chain in Figure 12. The frequency response was measured using a Zurich Instruments HF2LI lock-in amplifier by applying the excitation signal to a piezoelectric actuator attached to the AFM probe holder. The resulting sine sweeps with an excitation voltage of 10 mV are shown in Figure 13(a).

The noise measurement was performed by a National Instruments PXI system using a PXIe-6124 digitiser. An SRS SR560 preamplifier provided a gain of 2000 with a 10-kHz cutoff high-pass response. The LabView spectrum analysis tool was used to record the noise spectrum. A sample rate of 2 MS/s was used, and 20000 averages were collected. While measuring the noise spectrum, the piezoelectric chip was short circuited. The measured noise spectrum is shown in Figure 13(b), which shows the mechanical thermal noise of the cantilever at 352.8 kHz, and a noise floor of 70 fm/$\sqrt{\text{Hz}}$.

An oscilloscope was used to record large signal responses and to calibrate the interferometer. For example, when excited at its resonance frequency, the microcantilever oscillation is plotted in Figure 14. The calibration and initialization processes require the minimum and maximum values of the interferogram. The midpoint is used as the

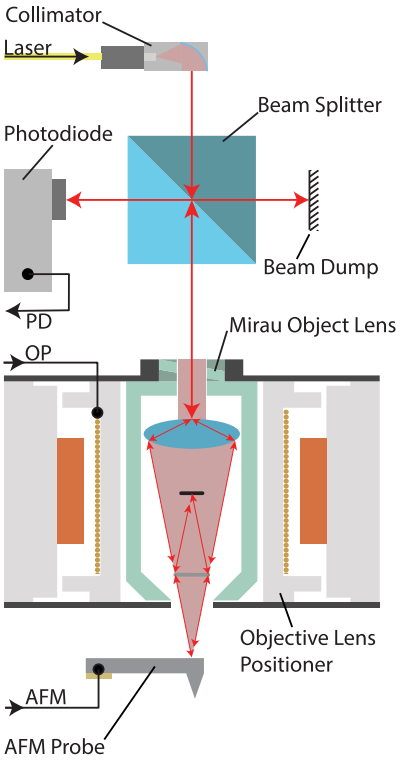

Fig. 11. Optical path of the phased-locked Michelson interferometer. 'PD' is the photodiode signal, 'OP' is the coil driving current, and 'AFM' is the excitation signal applied to the piezoelectric actuator in the microcantilever mount.

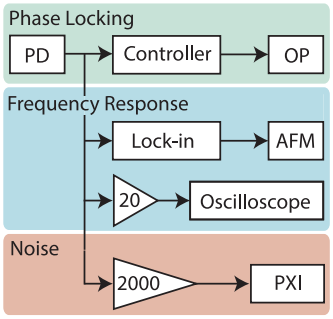

Fig. 12. Signal diagram of the phase-locked Michelson interferometer. 'PD' is the photodiode signal, 'OP' is the coil driving current, and 'AFM' is the excitation signal applied to the piezoelectric actuator in the microcantilever mount.

controller setpoint, and the peak-to-peak value is used to calculate the sensitivity. When operating at a zero crossing, the interferometer's sensitivity is $\lambda/2 \times \pi \times V_{pp}$, where λ is the laser wavelength, and V_{pp} is the peak-to-peak voltage of the interferogram [36].

The frequency response and noise measurement in Figure 13 indicate that the probe has a resonance frequency of 352.8 kHz, which is within specifications for the N15/AlBS 256-400 kHz AFM probe used in the experiments. For frequencies above 300 kHz, the noise floor is approximately 20 fm/$\sqrt{\text{Hz}}$, while the peak thermal noise of the microcantilever is 280 fm/$\sqrt{\text{Hz}}$. These results, combined with the 1 μm spot size possible with the 0.3 NA objective, show

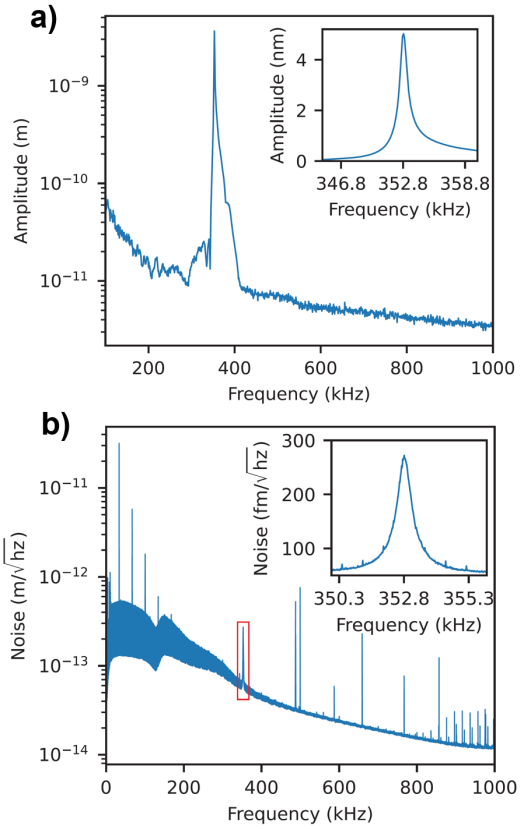

Fig. 13. (a) Measured frequency response of the intererometer-based AFM system. (b) Noise density spectrum of the Michelson interferometer system.

that the proposed objective lens scanner can successfully be integrated into an interferometer-based AFM that utilizes miniature high-frequency probes.

VII. Conclusions

This article describes a vertical objective scanner driven by a voice coil actuator for high-speed positioning applications. The travel range, stiffness and resonance frequency are derived analytically and closely match finite-element simulations and experimental results. The objective scanner has a travel range of 314 μm, a first resonance frequency of 106.9 Hz, less than 3.3% lateral cross-coupling, and less than 2% hysteresis. The objective scanner is successfully demonstrated in a phase-locked Michelson interferometer to measure the frequency response and thermal mechanical noise of a microcantilever.

Compared to existing piezoelectric objective scanners, the proposed electromagnetic objective scanner is insensitive to shock and vibration, is highly linear in open-loop, requires only low voltages, and can easily be reconfigured by changing the flexure. The disadvantages compared to a piezoelectric scanner include heat dissipation for static displacements, the possibility of stray magnetic fields, potentially lower lateral stiffness, and larger physical size.

References

[1] L. Zhu, Y. Dong, Z. Li, and X. Zhang, "A novel surface recovery algorithm for dual wavelength white led in vertical

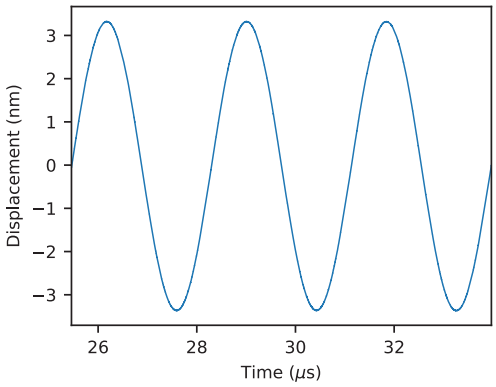

Fig. 14. Measured displacement of the AFM probe excited near its resonant frequency at 352.8 kHz. The interferometer measurement noise is not discernible over the 6.8 nm range.

scanning interferometry (VSI)," vol. 20, no. 18. [Online]. Available: https://www.mdpi.com/1424-8220/20/18/5225

[2] X. Guo, T. Guo, and L. Yuan, "Measurement of film structure using time-frequency-domain fitting and white-light scanning interferometry," vol. 9, no. 12. [Online]. Available: https://www.mdpi.com/2075-1702/9/12/336

[3] P. de Groot, "Interferometric methods of 3D surface structure analysis," in *11th Euro-American Workshop on Information Optics*, 2012, pp. 1–3.

[4] M. G. Lee, G. Kim, C.-W. Lee, S.-H. Lee, and Y. Jeon, "Design of voice coil motor dynamic focusing unit for a laser scanner," vol. 85, no. 4, p. 045104. [Online]. Available: https://doi.org/10.1063/1.4869339

[5] J. Xie, L. You, S. Huang, Z. Duan, and G. Chen, "Real-time focus control in broad flat field laser material processing," vol. 40, no. 2, pp. 330–336. [Online]. Available: https://www.sciencedirect.com/science/article/pii/S003039920700093X

[6] M. Lee, S. Kannan, G. Muniraj, V. Rosa, W. F. Lu, J. Y. Fuh, G. Sriram, and T. Cao, "Two-photon fluorescence microscopy and applications in angiogenesis and related molecular events," vol. 28, no. 4, pp. 926–937, pMID: 34541887. [Online]. Available: https://doi.org/10.1089/ten.teb.2021.0140

[7] N. Kojic, A. Huang, E. Chung, D. Tschumperlin, and P. T. C. So, "Quantification of three-dimensional dynamics of intercellular geometry under mechanical loading using a weighted directional adaptive-threshold method," vol. 16, no. 16, pp. 12 403–12 414. [Online]. Available: https://opg.optica.org/oe/abstract.cfm?URI=oe-16-16-12403

[8] C. M. Sutton and M. T. Clarkson, "A magnet system for the msl watt balance," vol. 51, no. 2, p. S101. [Online]. Available: https://dx.doi.org/10.1088/0026-1394/51/2/S101

[9] S. Kang, Y.-G. Jeong, and Y.-M. Choi, "Design of a Finger-Sized Voice Coil Motor for High-Speed Scanners," *International Journal of Precision Engineering and Manufacturing*, vol. 24, no. 2, pp. 209–217. [Online]. Available: https://doi.org/10.1007/s12541-022-00749-5

[10] Physik Instrumente Group, see https://www.physikinstrumente.com/en for their objective scanners.

[11] Thorlabs, Inc., see http://www.thorlabs.com/ for their nanopositioners.

[12] Prior Scientific, see https://www.prior.com/ for their objective scanners.

[13] CoreMorrow, see http://www.coremorrow.com/en for their objective scanners.

[14] Z. Chen, Y. Qiu, X. Zhong, and X. Zhang, "An xyz parallel nanopositioning stage with hybrid damping," *Sensors and Actuators A: Physical*, vol. 377, p. 115688, 2024. [Online]. Available: https://www.sciencedirect.com/science/article/pii/S0924424724006824

[15] Y. K. Yong and A. J. Fleming, "High-speed vertical positioning stage with integrated dual-sensor arrangement," *Sensors & Actuators: A. Physical*, vol. 248, pp. 184–192, 2016.

[16] Y. K. Yong, T.-F. Lu, and D. C. Handley, "Loop closure theory in deriving linear and simple kinematic model for a 3 DOF parallel micromanipulator," in *Device and Process Technologies for MEMS, Microelectronics, and Photonics III*, J.-C. Chiao, A. J. Hariz, D. N. Jamieson, G. Parish, and V. K. Varadan, Eds., vol. 5276, International Society for Optics and Photonics. SPIE, pp. 57 – 66. [Online]. Available: https://doi.org/10.1117/12.522258

[17] X. Zhao, F. Wang, B. Shi, Y. Tian, and D. Zhang, "A piezo-actuated nanopositioning stage based on spatial parasitic motion principle," *Sensors and Actuators A: Physical*, vol. 368, p. 115124, 2024. [Online]. Available: https://www.sciencedirect.com/science/article/pii/S0924424724001171

[18] R. Xu, Z. Wang, M. Zhou, and D. Tian, "A robust fractional-order sliding mode control technique for piezoelectric nanopositioning stages in trajectory-tracking applications," *Sensors and Actuators A: Physical*, vol. 363, p. 114711, 2023. [Online]. Available: https://www.sciencedirect.com/science/article/pii/S0924424723005605

[19] S. Ito, S. Troppmair, B. Lindner, F. Cigarini, and G. Schitter, "Long-range fast nanopositioner using nonlinearities of hybrid reluctance actuator for energy efficiency," *IEEE Transactions on Industrial Electronics*, vol. 66, no. 4, pp. 3051–3059, 2019.

[20] Y. K. Yong, "A new preload mechanism for a high-speed piezoelectric stack nanopositioner," *Mechatronics*, vol. 36, pp. 159 – 166, 2016.

[21] Y. K. Yong and S. O. R. Moheimani, "A compact XYZ scanner for fast atomic force microscopy in constant force contact mode," in *IEEE/ASME International Conference on Advanced Intelligent Mechatronics*, Montreal, Canada, July 6-9 2010, pp. 225–230.

[22] Y. K. Yong, S. O. R. Moheimani, B. J. Kenton, and K. K. Leang, "Invited review article: High-speed flexure-guided nanopositioning: Mechanical design and control issues," *Review of Scientific Instruments*, vol. 83, no. 12, p. 121101, 2012.

[23] W. Zhang and P. Yan, "A variable stiffness compliant actuator based on antagonistic normal-stressed electromagnetic mechanism," *Sensors and Actuators A: Physical*, vol. 366, p. 114983, 2024. [Online]. Available: https://www.sciencedirect.com/science/article/pii/S0924424723008324

[24] X. Wang, L. Li, Z. Zhu, and L. Zhu, "Simultaneous damping and tracking control of a normal-stressed electromagnetic actuated nano-positioning stage," *Sensors and Actuators A: Physical*, vol. 338, p. 113467, 2022. [Online]. Available: https://www.sciencedirect.com/science/article/pii/S0924424722001054

[25] S. Ito, F. Cigarini, and G. Schitter, "Flux-controlled hybrid reluctance actuator for high-precision scanning motion," *IEEE Transactions on Industrial Electronics*, vol. 67, no. 11, pp. 9593–9600, 2020.

[26] C.-L. Hsieh and C.-S. Liu, "Design of a voice coil motor actuator with l-shape coils for optical zooming smartphone cameras," *IEEE Access*, vol. 8, pp. 20 884–20 891, 2020.

[27] Y. K. Yong, S. Wadikhaye, and A. J. Fleming, "High-speed single-stage and dual-stage vertical positioners," *Review of Scientific Instruments*, vol. 87, no. 085104, pp. (1–8), 2016.

[28] Y. K. Yong and S. O. R. Moheimani, "Design of an inertially counter-balanced Z-nanopositioner for high-speed atomic force microscopy," *IEEE/ASME Transactions on Nanotechnology*, vol. 12, no. 2, pp. 137 – 145, 2013.

[29] B. J. Kenton, A. J. Fleming, and K. K. Leang, "Compact ultra-fast vertical nanopositioner for improving scanning probe microscope scan speed," *Review of Scientific Instruments*, vol. 82, no. 12, p. 123703, 2011.

[30] N. Lobontiu, *Compliant Mechanisms: Design of flexure hinges*. CRC Press, 2003.

[31] A. J. Fleming and Y. K. Yong, "An ultrathin monolithic XY nanopositioning stage constructed from a single sheet of piezoelectric material," *IEEE/ASME Transactions on Mechatronics*, vol. 22, no. 6, pp. 2611–2618, Dec 2017.

[32] T. Dahlberg, "Procedure to calculate deflections of curved beams," *The International Journal of Engineering Education*, vol. 20, no. 3, pp. 503–513, 2004.

[33] W. Thomson, *Theory of Vibration with Applications*, 3rd ed. Prentice-Hall, Englewood Cliffs, 1988.

[34] B. S. Guru and H. R. Hiziroglu, *Electric machinery and transformers*. Oxford university press New York, 2001, vol. 726.

[35] "N35 material datasheet for sintered neodymium-iron-boron magnets."

[36] A. J. Fleming and B. S. Routley, "A closed-loop phase-locked interferometer for wide bandwidth position sensing," *Review of Scientific Instruments*, vol. 86, no. 11, p. 115001, 11 2015. [Online]. Available: https://doi.org/10.1063/1.4935469